

# 12

## SPRAYS

### 12.1 INTRODUCTION

Sprays are an important constituent of many natural and technological processes and range in scale from the very large dimensions of the global air-sea interaction and the dynamics of spillways and plunge pools to the smaller dimensions of fuel injection and ink jet systems. In this chapter we first examine the processes by which sprays are formed and some of the resulting features of those sprays. Then since, the the combustion of liquid fuels in droplet form constitute such an important component of our industrialized society, we focus on the evaporation and combustion of single droplets and follow that with an examination of the features involved in the combustion of sprays.

### 12.2 TYPES OF SPRAY FORMATION

In general, sprays are formed when the interface between a liquid and a gas becomes deformed and droplets of liquid are generated. These then migrate out into the body of the gas. Sometimes the gas plays a negligible role in the kinematics and dynamics of the droplet formation process; this simplifies the analyses of the phenomena. In other circumstances the gasdynamic forces generated can play an important role. This tends to occur when the relative velocity between the gas and the liquid becomes large as is the case, for example, with hurricane-generated ocean spray.

Several prototypical flow geometries are characteristic of the natural and technological circumstances in which spray formation is important. The first prototypical geometry is the flow of a gas over a liquid surface. When the relative velocity is sufficiently large, the interfacial shear stress produces waves on the interface and the breakup of the waves generates a spray that

is transported further into the gas phase by the turbulent motions. Ocean spray generated in high wind conditions falls into this category as does annular, vertical two-phase flow. In some fuel injectors a coflowing gas jet is often added to enhance spray formation. Section 12.4.2 provides an overview of this class of spray formation processes.

A second, related configuration is a liquid pool or ocean into which gas is injected so that the bubbles rise up to break through the free surface of the liquid. In the more quiescent version of this configuration, the spray is formed by process of break-through (see section 12.4.1). However, as the superficial gas flux is increased, the induced liquid motions become more violent and spray is formed within the gas bubbles. This spray is then released when the bubbles reach the surface. An example of this is the spray contained within the gas phase of churn-turbulent flow in a vertical pipe.

A third configuration is the formation of a spray due to condensation in a vapor flow. This process is governed by a very different set of physical principles. The nucleation mechanisms involved are beyond the scope of this book.

The fourth configuration is the break up of a liquid jet propelled through a nozzle into a gaseous atmosphere. The unsteady, turbulent motions in the liquid (or the gas) generate ligaments of liquid that project into the gas and the breakup of these ligaments creates the spray. The jet may be laminar or turbulent when it leaves the nozzle and the details of ligament formation, jet breakup and spray formation are somewhat different in the two cases. Sections 12.4.3 and 12.4.4 will summarize the processes of this flow configuration.

One area in which sprays play a very important role is in the combustion of liquid fuels. We conclude this chapter with brief reviews of the important phenomena associated with the combustion of sprays, beginning with the evaporation of droplets and concluding with droplet and droplet cloud combustion.

### 12.3 OCEAN SPRAY

Before proceeding with the details of the formation of spray at a liquid/gas interface, a few comments are in order regarding the most widely studied example, namely spray generation on the ocean surface. It is widely accepted that the mixing of the two components, namely air and water, at the ocean surface has important consequences for the global environment (see, for example, Liss and Slinn, 1983, or Kraus and Businger, 1994). The heat and

mass exchange processes that occur as a result of the formation of bubbles in the ocean and of droplets in the atmosphere are critical to many important global balances, including the global balances of many gases and chemicals. For example, the bubbles formed by white caps play an important role in the oceanic absorption of carbon dioxide; on the other side of the interface the spray droplets form salt particles that can be carried high into the atmosphere. They, in turn, are an important contributor to condensation nuclei. Small wonder, then, that ocean surface mixing, the formation of bubbles and droplets, have been extensively studied (see for example Monahan and Van Patten, 1989). But the mechanics of these processes are quite complicated, involving as they do, not only the complexity of wave formation and breaking but the dynamics of turbulence in the presence of free surfaces. This, in turn, may be affected by free surface contamination or dissolved salts because these effect the surface tension and other free surface properties. Thus, for example, the bubble and droplet size distributions formed in salt water are noticeably different from those formed in fresh water (Monahan and Zietlow, 1969). Here, we shall not attempt a comprehensive review of this extensive literature but confine ourselves to some of the basic mechanical processes that are believed to influence these oceanic phenomena.

There appears to be some general concensus regarding the process of spray formation in the ocean (Blanchard, 1983, Monahan, 1989). This holds that, at relatively low wind speeds, the dominant droplet spray is generated by bubbles rising to breach the surface. The details of the droplet formation process are described in greater detail in the next section. The most prolific source of bubbles are the white caps that can cover up to 10% of the ocean surface (Blanchard, 1963). Consequently, an understanding of the droplet formation requires an understanding of bubble formation in breaking waves; this, in itself, is a complex process as illustrated by Wood (1991). What is less clear is the role played by wind shear in ocean spray formation (see section 12.4.2).

Monahan (1989) provides a valuable survey and rough quantification of ocean spray formation, beginning with the white cap coverage and proceeding through the bubble size distributions to some estimate of the spray size distribution. Of course, the average droplet size decays with elevation above the surface as the larger droplets settle faster; thus, for example, de Leeuw (1987) found the average droplet diameter at a wind speed of  $5.5\text{m/s}$  dropped from  $18\mu\text{m}$  at an elevation of  $2\text{m}$  to  $15\mu\text{m}$  at  $10\text{m}$  elevation. The size also increases with increasing wind speed due to the greater turbulent velocities in the air.

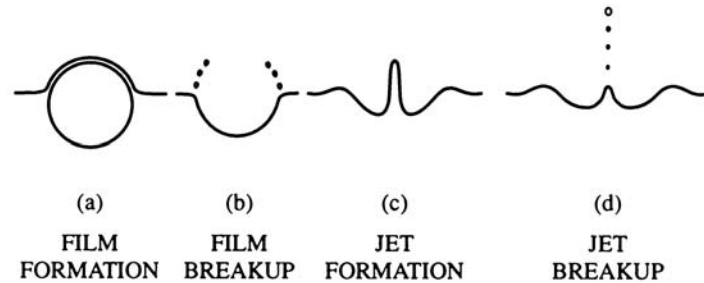


**Figure 12.1.** Stages of a bubble breaking through a free surface.

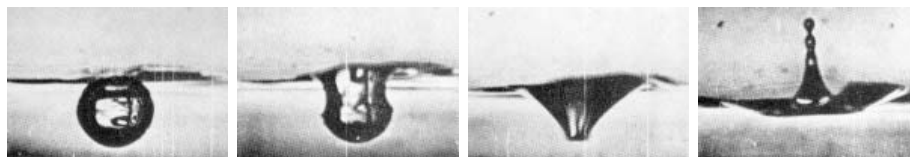


**Figure 12.2.** Photographs by Blanchard (1963) of a bubble breaking through a free surface. Reproduced with permission of the author.

It is also important to observe that there are substantial differences between spray formation in the ocean and in fresh water. The typical bubbles formed by wave breaking are much smaller in the ocean though the total bubble volume is similar (Wang and Monahan, 1995). Since the bubble size determines the droplet size created when the bubble bursts through the surface, it follows that the spray produced in the ocean has many more, smaller droplets. Moreover, the ocean droplets have a much longer lifetime. Whereas fresh water droplets evaporate completely in an atmosphere with less than 100% relative humidity, salt water droplets increase their salinity with evaporation until they reach equilibrium with their surroundings. Parenthetically, it is interesting to note that somewhat similar differences have been observed between cavitation bubbles in salt water and fresh water (Ceccio *et al.* 1997); the bubbles in salt water are smaller and more numerous.

## 12.4 SPRAY FORMATION

### 12.4.1 *Spray formation by bubbling*

When gas bubbles rise through a pool of liquid and approach the free surface, the various violent motions associated with the break through to the cover gas generate droplets that may persist in the cover gas to constitute a spray.

Even in an otherwise quiescent liquid, the details of the bubble breakthrough are surprisingly complicated as illustrated by the photographs in figure 12.2. Two of the several important processes are sketched in figure 12.1. Just prior to breakthrough a film of liquid is formed on the top of the bubble and the disintegration of this film creates one set of droplets. After breakthrough, as surface waves propagate inward (as well as outward) an upward jet is formed in the center of the disruption and the disintegration of this jet also creates droplets. Generally, the largest *jet droplets* are substantially larger than the largest *film droplets*, the latter being about a tenth the diameter of the original bubble.

In both the industrial and oceanic processes, a key question is the range of droplet sizes that will almost immediately fall back into the liquid pool and, on the other hand, the range of droplet sizes that will be carried high into the atmosphere or cover gas. In the ocean this significant transport above the water surface occurs as a result of turbulent mixing. In the industrial context of a liquid-fluidized bed, the upward transport is often the result of a sufficiently large upward gas flux whose velocity in the cover space exceeds the settling velocity of the droplet (Azbel and Liapis, 1983).

#### 12.4.2 *Spray formation by wind shear*

In annular flows in vertical pipes, the mass of liquid carried as droplets in the gas core is often substantial. Consequently considerable effort has been devoted to studies of the entrainment of droplets from the liquid layer on the pipe wall (Butterworth and Hewitt, 1977, Whalley 1987). In many annular flows the droplet concentration in the gas core increases with elevation as illustrated in figure 12.3.

In steady flow, the mass flux of droplets entrained into the gas core,  $G_L^E$  should be balanced by the mass flux of deposition of droplets onto the wall liquid layer,  $G_L^D$ . Hutchinson and Whalley (1973) observe that droplets are torn from the liquid surface when the wind shear creates and then fractures a surface wave as sketched in figure 12.4. They suggest that the velocity of ejection of the droplets is related to the friction velocity,  $u^* = (\tau_i/\rho_L)^{\frac{1}{2}}$ , where  $\tau_i$  is the interfacial stress and that the entrainment rate,  $G_L^E$ , therefore correlates with  $(\tau_i\delta/S)^{\frac{1}{2}}$ , where  $\delta$  is the mean liquid layer thickness. They also speculate that the mass deposition rate must be proportional to the core droplet mass concentration,  $\rho_L\alpha_L$ . As shown in figure 12.5, the experimental measurements of the concentration do, indeed, appear to correlate

with  $(\tau_i \delta / S)^{\frac{1}{2}}$  (a typical square root dependence is shown by the solid line in the figure).

McCoy and Hanratty (1977) review the measurements of the deposition mass flux,  $G_L^D$ , and the gas core concentration,  $\rho_L \alpha_L$ , and show that the dimensionless deposition mass transfer coefficient,  $G_L^D / \rho_L \alpha_L u^*$ , correlates with a dimensionless relaxation time for the droplets defined by  $D^2 \rho_L \rho_G u^{*2} / 18 \mu_G^2$ . This correlation is shown in figure 12.6 and, for a given  $u^*$ , can also be considered as a graph with the resulting droplet size,  $D$  (or

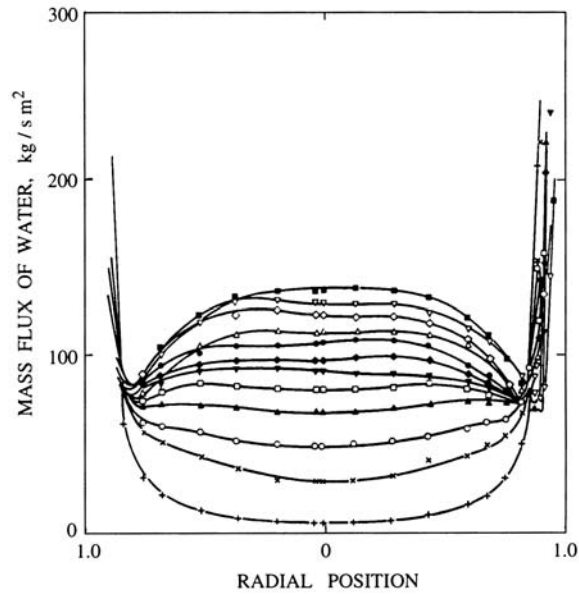


**Figure 12.3.** Droplet concentration profiles in the gas core of a vertical annular pipe flow (3.2cm diameter) illustrating the increase with elevation from initiation (lowest line, 15cm elevation; uppermost line, 531cm elevation) (from Gill *et al.* 1963).

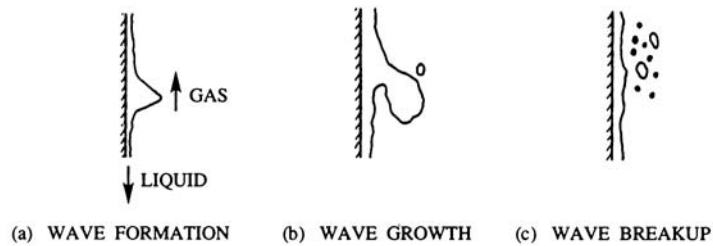


**Figure 12.4.** Sketch illustrating the ejection of droplets by wind shear in annular flow in a vertical pipe. From Hutchinson and Whalley (1973).

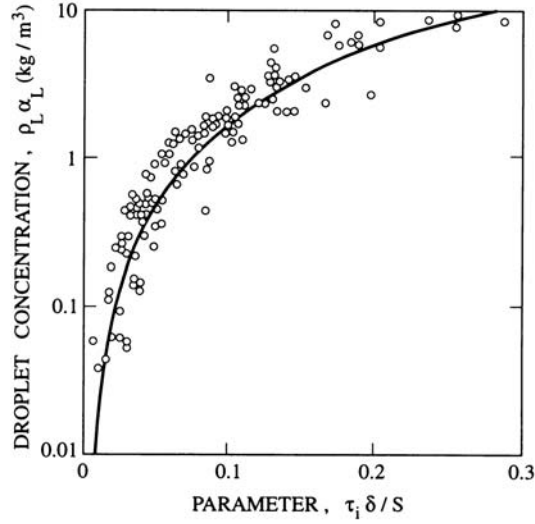


**Figure 12.5.** The mass concentration of liquid droplets in the gas core of an annular flow,  $\rho_L \alpha_L$ , plotted against  $\tau_i \delta / S$ . From Hutchinson and Whalley (1973).

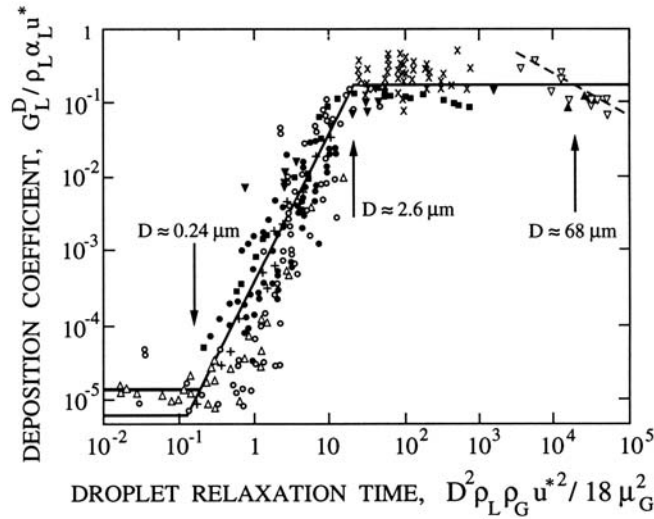


**Figure 12.6.** The dimensionless deposition mass transfer coefficient,  $G_L^D / \rho_L \alpha_L u^*$ , for vertical annular flow plotted against a dimensionless relaxation time for the droplets in the core,  $D^2 \rho_L \rho_G u^{*2} / 18 \mu_G^2$ . A summary of experimental data compiled by McCoy and Hanratty (1977).

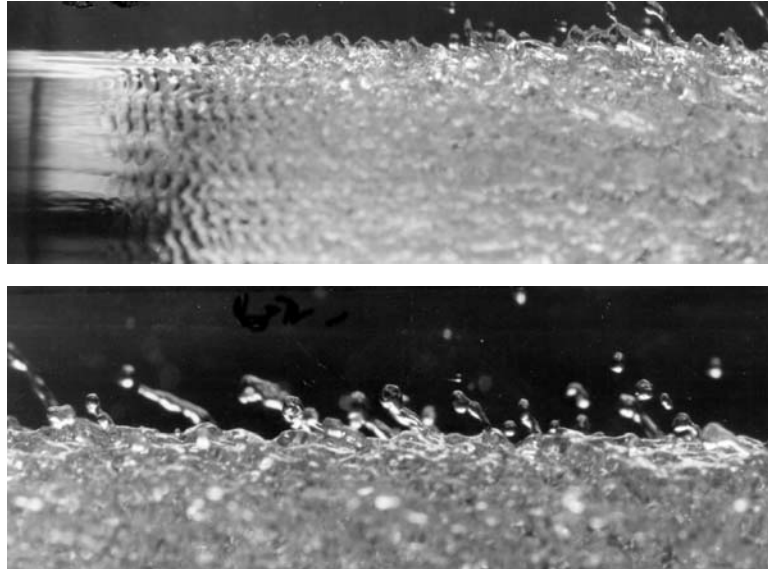


**Figure 12.7.** Photographs of an initially laminar jet emerging from a nozzle. The upper photograph shows the instability wave formation and growth and the lower shows the spray droplet formation at a location 4 diameters further downstream. Figure 12.9 shows the same jet even further downstream. Reproduced from Hoyt and Taylor (1977b) with the permission of the authors.

rather its square), plotted horizontally; typical droplet sizes are shown in the figure.

### *12.4.3 Spray formation by initially laminar jets*

In many important technological processes, sprays are formed by the breakup of a liquid jet injected into a gaseous atmosphere. One of the most important of these, is fuel injection in power plants, aircraft and automobile engines and here the character of the spray formed is critical not only for performance but also for pollution control. Consequently much effort has gone into the design of the nozzles (and therefore the jets) that produce sprays with desirable characteristics. *Atomizing* nozzles are those that produce particularly fine sprays. Other examples of technologies in which there is a similar focus on the nature of the spray produced are ink-jet printing and the *scrubbing* of exhaust gases to remove particulate pollutants.

Because of its technological importance, we focus here on the circumstance in which the jet is turbulent when it emerges from the nozzle. How-

ever, in passing, we note that the breakup of laminar jets may also be of interest. Two photographs of initially laminar jets taken by Hoyt and Taylor (1977a,b) are reproduced in figure 12.7. Photographs such as the upper one clearly show that transition to turbulence occurs because the interfacial layer formed when the liquid boundary layer leaves the nozzle becomes unstable. The Tollmein-Schlichting waves (remarkably two-dimensional) exhibit a well-defined wavelength and grow to non-linear amplitudes at which they breakup to form droplets in the gas. Sirignano and Mehring (2000) provide a review of the extensive literature on linear and non-linear analyses of the stability of liquid jets, not only round jets but also planar and annular jets. The author (Brennen 1970) examined the development of interfacial instability waves in the somewhat different context of cavity flows; this analysis demonstrated that the appropriate length scale is the thickness of the internal boundary layer,  $\delta$ , on the nozzle walls at the point where the free surface detaches. This is best characterized by the momentum thickness,  $\delta_2$ , though other measures of the boundary layer thickness have also been used. The stability analysis yields the most unstable wavelength for the Tollmein-Schlichting waves (normalized by  $\delta_2$ ) as a function of the Reynolds number of the interfacial boundary layer (based on the jet velocity and  $\delta_2$ ). At larger Reynolds number, the ratio of wavelength to  $\delta_2$  reaches an asymptotic value of about 25, independent of Reynolds number. Brennen (1970) and Hoyt and Taylor (1977a,b) observe that these predicted wavelengths are in accord with those observed.

A natural extension of this analysis is to argue that the size of the droplets formed by the non-linear breakup of the instability waves will scale with the wavelength of those waves. Indeed, the pictures of Hoyt and Taylor (1977a,b) exemplified by the lower photograph in figure 12.7 suggest that this is the case. It follows that at higher Reynolds numbers, the droplet size should scale with the boundary layer thickness,  $\delta_2$ . Wu, Miranda and Faeth (1995) have shown that this is indeed the case for the initial drop formation in initially nonturbulent jets.

Further downstream the turbulence spreads throughout the core of the jet and the subsequent jet breakup and droplet formation is then similar to that of jets that are initially turbulent. We now turn to that circumstance.

#### *12.4.4 Spray formation by turbulent jets*

Because of the desirability in many technological contexts of nozzles that produce jets that are fully turbulent from the start, there has been extensive testing of many nozzle designed with this objective in mind. Simmons (1977)

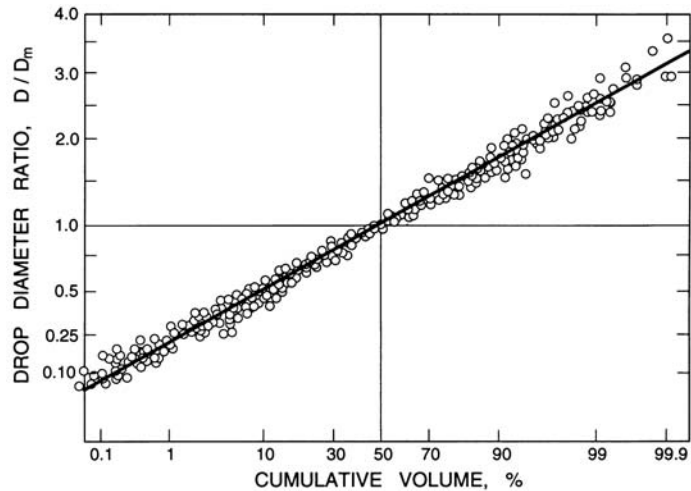


**Figure 12.8.** The distribution of droplet sizes in sprays from many types of nozzles plotted on a root/normal graph. Adapted from Simmons (1977).

makes the useful observation that sprays produced by a wide range of nozzle designs have similar droplet size distributions when these are compared in a *root/normal* graph as shown in figure 12.8. Here the ordinate corresponds to  $(D/D_m)^{\frac{1}{2}}$  where  $D_m$  is the mass mean diameter (see section 1.1.4). The horizontal scale is stretched to correspond to a normal distribution. The straight line to which all the data collapse implies that  $(D/D_m)^{\frac{1}{2}}$  follows a normal distribution. Since the size distributions from many different nozzles all have the same form, this implies that the sprays from all these nozzles can be characterized by a single diameter,  $D_m$ . An alternative measure is the Sauter mean diameter,  $D_s$ , since  $D_s/D_m$  will have the universal value of 1.2 under these circumstances.

Early studies of liquid jets by Lee and Spencer (1933) and others revealed that the turbulence in a liquid jet was the primary initiator of break-up. Subsequent studies (for example, Phinney 1973, Hoyt and Taylor 1977a,b, Ervine and Falvey 1987, Wu *et al.* 1995, Sarpkaya and Merrill 1998) have examined how this process works. In the early stages of breakup, the turbulent structures in the jet produce ligaments that project into the gaseous phase and then fragment to form droplets as illustrated in figure 12.7. The studies by Wu *et al.* (1995) and others indicate that the very smallest structures in the turbulence do not have the energy to overcome the restraining forces of surface tension. However, since the smaller turbulent structures distort the free surface more rapidly than the larger structures, the first ligaments and droplets to appear are generated by the smallest scale structures

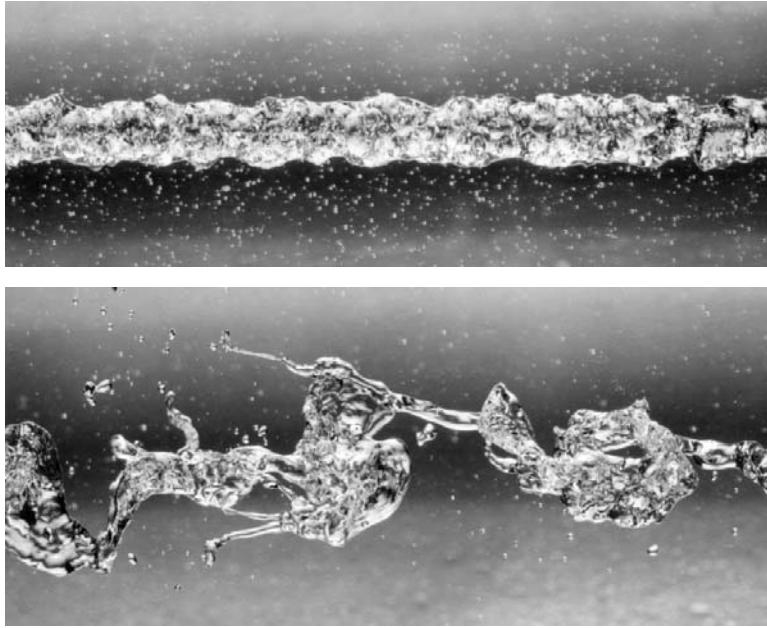


**Figure 12.9.** A continuation from figure 12.7 showing two further views of the jet at 72 diameters (above) and 312 diameters (below) downstream from the nozzle. The latter illustrates the final breakup of the jet. Reproduced from Hoyt and Taylor (1977b) with the permission of the authors.

that *are* able to overcome surface tension. This produces small droplets. But these small structures also decay more rapidly with distance from the nozzle. Consequently, further downstream progressively larger structures cause larger ligaments and droplets and therefore add droplets at the higher end of the size distribution. Finally, the largest turbulent structures comparable with the jet diameter or width initiate the final stage of jet decomposition as illustrated in figure 12.9.

Wu, Miranda and Faeth (1995) utilized this understanding of the spray formation and jet breakup process to create scaling laws of the phenomenon. With a view to generalizing the results to turbulent jets of other cross-sections, the radial integral length scale of the turbulence is denoted by  $4\Lambda$  where, in the case of round jets,  $\Lambda = d_j/8$ , where  $d_j$  is the jet diameter. Wu *et al.* (1995) then argue that the critical condition for the initial formation of a droplet (the so-called primary breakup condition) occurs when the kinetic energy of a turbulent eddy of the critical size is equal to the surface energy required to form a droplet of that size. This leads to the following expression

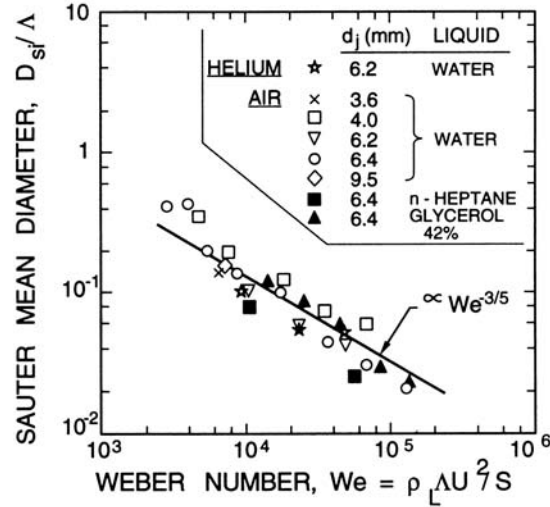


**Figure 12.10.** The Sauter mean diameter,  $D_{si}$ , of the initial droplets formed (divided by the typical dimension of the jet,  $\Lambda$ ) in turbulent round jets as a function of the Weber number,  $We = \rho_L \Lambda U^2 / S$ . The points are experimental measurements for various liquids and jet diameters,  $d_j$ . Adapted from Wu *et al.* (1995).

for the Sauter mean diameter of the initial droplets,  $D_{si}$ :

$$\frac{D_{si}}{\Lambda} \propto We^{-\frac{3}{5}} \quad (12.1)$$

where the Weber number,  $We = \rho_L \Lambda U^2$ ,  $U$  being the typical or mean velocity of the jet. Figure 12.10 from Wu *et al.* (1995) demonstrates that data from a range of experiments with round jets confirm that  $D_{si}/\Lambda$  does appear to be a function only of  $We$  and that the correlation is close to the form given in equation 12.1.

Wu *et al.* (1995) further argue that the distance,  $x_i$ , from the nozzle to the place where primary droplet formation takes place may be estimated using an eddy convection velocity equal to  $U$  and the time required for Rayleigh breakup of a ligament having a diameter equal to the  $D_{si}$ . This leads to

$$\frac{x_i}{\Lambda} \propto We^{-\frac{2}{5}} \quad (12.2)$$

and, as shown in figure 12.11, the data for different liquids and jet diameters are in rough accord with this correlation.

Downstream of the point where primary droplet formation occurs, progressively larger eddies produce larger droplets and Wu *et al.* (1995) use extensions of their theory to generate the following expression for the Sauter

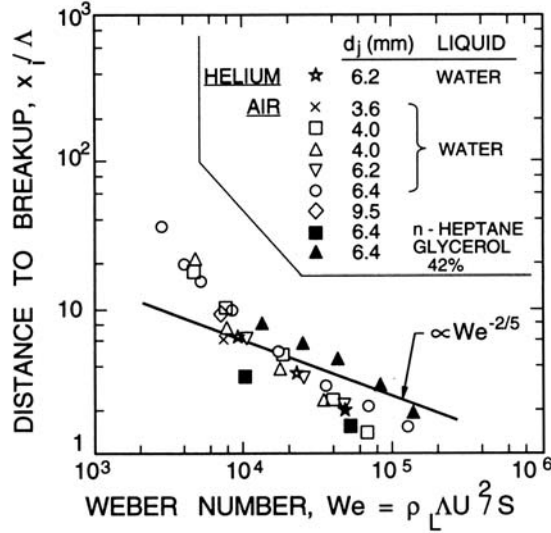


**Figure 12.11.** The ratio of the distance from the nozzle to the point where turbulent breakup begins (divided by  $\Lambda$ ) for turbulent round jets as a function of the Weber number,  $We = \rho_L \Delta U^2 / S$ . The points are experimental measurements for various liquids and jet diameters,  $d_j$ . Adapted from Wu *et al.* (1995).

mean diameter,  $D_s$ , of the droplets formed at a distance,  $x$ , downstream of the nozzle:

$$\frac{D_s}{\Lambda} \propto \left( \frac{x}{\Lambda We^{1/2}} \right)^{2/3} \quad (12.3)$$

As shown in figure 12.12 the experimental measurements show fair agreement with this approximate theory.

Using this information, the evolution of the droplet size distribution with distance from the nozzle can be constructed as follows. Assuming Simmons size distributions, the droplet size distribution may be characterized by the Sauter mean diameter,  $D_s$ . The primary breakup yields droplets characterized by the initial  $D_{si}$  of equation 12.1. Then, moving downstream along the jet, contributions with progressively larger droplets are added until the jet finally disintegrates completely.

Several footnotes should be added to this picture. First, the evolution described assumes that the gaseous phase plays a negligible role in the dynamics. Wu and Faeth (1993) demonstrate that this will only be the case when  $\rho_L / \rho_G > 500$ . However this is frequently the case in practical applications. Second, the above can be extended to other free jet geometries. Dai

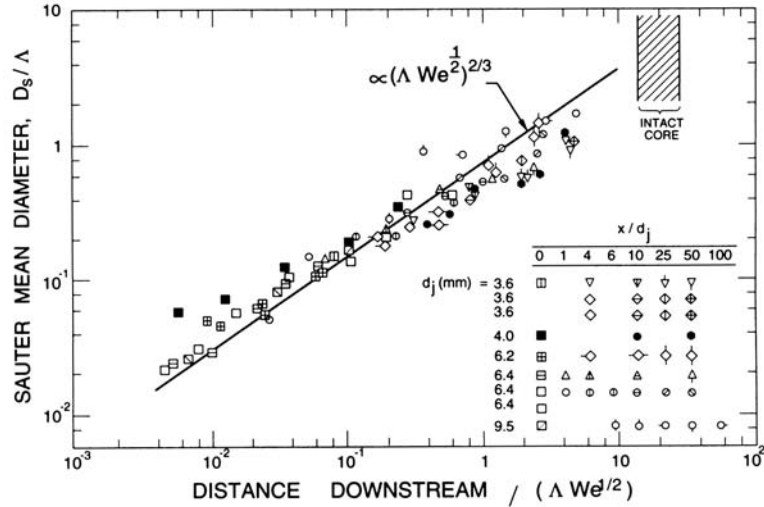


**Figure 12.12.** The Sauter mean diameter,  $D_s$  (divided by  $\Lambda$ ), of the droplets formed at a distance,  $x$ , from the nozzle for turbulent round jets for various Weber numbers,  $We = \rho_L \Lambda U^2 / S$ . The points are experimental measurements for various liquids and jet diameters,  $d_j$ . Adapted from Wu *et al.* (1995).

*et al.* (1998) demonstrate that the simple use of a hydraulic diameter allows the same correlations to be used for plane jets. On the other hand, wall jets appear to follow different correlations presumably because the generation of vorticity in wall jets causes a different evolution of the turbulence than occurs in free jets (Dai *et al.* 1997, Sarpkaya and Merrill 1998). Sarpkaya and Merrill's (1998) experiments with wall jets on horizontal smooth and roughened walls exhibit a ligament formation process qualitatively similar to that of free jets. The droplets created by the ligament breakup have a diameter about 0.6 of the wall jet thickness and quite independent of Weber number or plate roughness over the range tested.

Finally, the reader will note that the above characterizations are notably incomplete since they do not address the issue of the total number or mass of droplets produced at each stage in the process. Though this is crucial information in many technological contexts, it has yet to be satisfactorily modeled.

## 12.5 SINGLE DROPLET MECHANICS

### 12.5.1 Single droplet evaporation

The combustion of liquid fuels in droplet form or of solid fuels in particulate form constitute a very important component of our industrialized society. Spray evaporation is important, in part because it constitutes the first stage in the combustion of atomized liquid fuels in devices such as industrial furnaces, diesel engines, liquid rocket engines or gas turbines. Consequently the mechanics of the evaporation and subsequent combustion have been extensively documented and studied (see, for example, Williams 1965, Glassman 1977, Law 1982, Faeth 1983, Kuo 1986) and their air pollution consequences examined in detail (see, for example, Flagan and Seinfeld 1988). It is impossible to present a full review of these subjects within the confines of this book, but it is important and appropriate to briefly review some of the basic multiphase flow phenomena that are central to these processes.

An appropriate place to start is with evaporation of a single droplet in a quiescent environment and we will follow the description given in Flagan and Seinfeld (1988). Heat diffusing inward from the combustion zone, either one surrounding a gas/droplet cloud or one located around an individual droplet, will cause the heating and evaporation of the droplet(s). It transpires that it is adequate for most purposes to model single droplet evaporation as a steady state process (assuming the droplet radius is only varying slowly). Since the liquid density is much greater than the vapor density, the droplet radius,  $R$ , can be assumed constant in the short term and this permits a steady flow analysis in the surrounding gas. Then, since the outward flow of total mass and of vapor mass at every radius,  $r$ , is equal to  $\dot{m}_V$  and there is no net flux of the other gas, conservation of total mass and conservation of vapor lead through equations 1.21 and 1.29 and Fick's Law 1.37 to

$$\frac{\dot{m}_V}{4\pi} = \rho u r^2 = \rho (u)_{r=R} R^2 \quad (12.4)$$

and

$$\frac{\dot{m}_V}{4\pi} = \rho u r^2 x_V - \rho r^2 D \frac{dx_V}{dr} \quad (12.5)$$

where  $D$  is the mass diffusivity. These represent equations to be solved for the mass fraction of the vapor,  $x_V$ . Eliminating  $u$  and integrating produces

$$\frac{\dot{m}_V}{4\pi} = \rho R D \ln \left( 1 + \frac{(x_V)_{r=\infty} - (x_V)_{r=R}}{(x_V)_{r=R} - 1} \right) \quad (12.6)$$

Next we examine the heat transfer in this process. The equation governing

the radial convection and diffusion of heat is

$$\rho u c_p \frac{dT}{dr} = \frac{1}{r^2} \frac{d}{dr} \left( r^2 k \frac{dT}{dr} \right) \quad (12.7)$$

where  $c_p$  and  $k$  are representative averages of, respectively, the specific heat at constant pressure and the thermal conductivity of the gas. Substituting for  $u$  from equation 12.4 this can be integrated to yield

$$\dot{m}_V c_p (T + C) = 4\pi r^2 k \frac{dT}{dr} \quad (12.8)$$

where  $C$  is an integration constant that is evaluated by means of the boundary condition at the droplet surface. The heat required to vaporize a unit mass of fuel whose initial temperature is denoted by  $T_i$  is clearly that required to heat it to the saturation temperature,  $T_e$ , plus the latent heat,  $\mathcal{L}$ , or  $c_s(T_e - T_i) + \mathcal{L}$ . The second contribution is usually dominant so the heat flux at the droplet surface can be set as:

$$4\pi R^2 k \left( \frac{dT}{dr} \right)_{r=R} = \dot{m}_V \mathcal{L} \quad (12.9)$$

Using this boundary condition,  $C$  can be evaluated and equation 12.8 further integrated to obtain

$$\frac{\dot{m}_V}{4\pi} = \frac{Rk}{c_p} \ln \left\{ 1 + \frac{c_p(T_{r=\infty} - T_{r=R})}{\mathcal{L}} \right\} \quad (12.10)$$

To solve for  $T_{r=R}$  and  $(x_V)_{r=R}$  we eliminate  $\dot{m}_V$  from equations 12.6 and 12.10 and obtain

$$\frac{\rho D c_p}{k} \ln \left( 1 + \frac{(x_V)_{r=\infty} - (x_V)_{r=R}}{(x_V)_{r=R} - 1} \right) = \ln \left( 1 + \frac{c_p(T_{r=\infty} - T_{r=R})}{\mathcal{L}} \right) \quad (12.11)$$

Given the transport and thermodynamic properties  $k$ ,  $c_p$ ,  $\mathcal{L}$ , and  $D$  (neglecting variations of these with temperature) as well as  $T_{r=\infty}$  and  $\rho$ , this equation relates the droplet surface mass fraction,  $(x_V)_{r=R}$ , and temperature  $T_{r=R}$ . Of course, these two quantities are also connected by the thermodynamic relation

$$(x_V)_{r=R} = \frac{(\rho_V)_{r=R}}{\rho} = \frac{(p_V)_{r=R} \mathcal{M}_V}{p \mathcal{M}} \quad (12.12)$$

where  $\mathcal{M}_V$  and  $\mathcal{M}$  are the molecular weights of the vapor and the mixture. Equation 12.11 can then be solved given the relation 12.12 and the saturated vapor pressure  $p_V$  as a function of temperature. Note that since the droplet

size does not occur in equation 12.11, the surface temperature is independent of the droplet size.

Once the surface temperature and mass fraction are known, the rate of evaporation can be calculated from equation 12.7 by substituting  $\dot{m}_V = 4\pi\rho_L R^2 dR/dt$  and integrating to obtain

$$R^2 - (R_{t=0})^2 = \left\{ \frac{2k}{c_p} \ln \left( 1 + \frac{c_p(T_{r=\infty} - T_{r=R})}{\mathcal{L}} \right) \right\} t \quad (12.13)$$

Thus the time required for complete evaporation,  $t_{ev}$ , is

$$t_{ev} = c_p R_{t=0}^2 \left\{ 2k \ln \left( 1 + \frac{c_p(T_{r=\infty} - T_{r=R})}{\mathcal{L}} \right) \right\}^{-1} \quad (12.14)$$

This quantity is important in combustion systems. If it approaches the residence time in the combustor this may lead to incomplete combustion, a failure that is usually avoided by using atomizing nozzles that make the initial droplet size,  $R_{t=0}$ , as small as possible.

Having outlined the form of the solution for an evaporating droplet, albeit in the simplest case, we now proceed to consider the combustion of a single droplet.

### 12.5.2 Single droplet combustion

For very small droplets of a volatile fuel, droplet evaporation is completed early in the heating process and the subsequent combustion process is unchanged by the fact that the fuel began in droplet form. On the other hand for larger droplets or less volatile fuels, droplet evaporation will be a control-

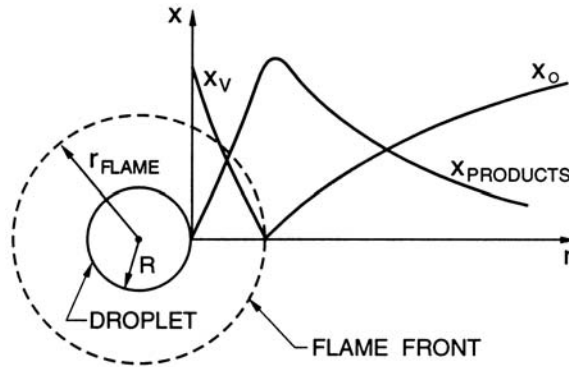


**Figure 12.13.** Schematic of single droplet combustion indicating the radial distributions of fuel/vapor mass fraction,  $x_V$ , oxidant mass fraction,  $x_O$ , and combustion products mass fraction.

ling process during combustion. Consequently, analysis of the combustion of a single droplet begins with the single droplet evaporation discussed in the preceding section. Then single droplet combustion consists of the outward diffusion of fuel vapor from the droplet surface and the inward diffusion of oxygen (or other oxidant) from the far field, with the two reacting in a flame front at a certain radius from the droplet. It is usually adequate to assume that this combustion occurs instantaneously in a thin *flame front* at a specific radius,  $r_{flame}$ , as indicated in figure 12.13. As in the last section, a steady state process will be assumed in which the mass rates of consumption of fuel and oxidant in the flame are denoted by  $\dot{m}_{VC}$  and  $\dot{m}_{OC}$  respectively. For combustion stoichiometry we therefore have

$$\dot{m}_{VC} = \nu \dot{m}_{OC} \quad (12.15)$$

where  $\nu$  is the mass-based stoichiometric coefficient for complete combustion. Moreover the rate of heat release due to combustion will be  $\mathcal{Q}\dot{m}_{VC}$  where  $\mathcal{Q}$  is the combustion heat release per unit mass of fuel. Assuming the mass diffusivities for the fuel and oxidant and the thermal diffusivity ( $k/\rho c_p$ ) are all the same (a Lewis number of unity) and denoted by  $D$ , the thermal and mass conservation equations for this process can then be written as:

$$\dot{m}_V \frac{dT}{dr} = \frac{d}{dr} \left( 4\pi r^2 \rho D \frac{dT}{dr} \right) + 4\pi r^2 \frac{\mathcal{Q}\dot{m}_{VC}}{c_p} \quad (12.16)$$

$$\dot{m}_V \frac{dx_V}{dr} = \frac{d}{dr} \left( 4\pi r^2 \rho D \frac{dx_V}{dr} \right) + 4\pi r^2 \dot{m}_{VC} \quad (12.17)$$

$$\dot{m}_V \frac{dx_O}{dr} = \frac{d}{dr} \left( 4\pi r^2 \rho D \frac{dx_O}{dr} \right) - 4\pi r^2 \dot{m}_{OC} \quad (12.18)$$

where  $x_O$  is the mass fraction of oxidant.

Using equation 12.15 to eliminate the reaction rate terms these become

$$\dot{m}_V \frac{d}{dr} (c_p T + \mathcal{Q}x_V) = \frac{d}{dr} \left( 4\pi r^2 \rho D \frac{d}{dr} (c_p T + \mathcal{Q}x_V) \right) \quad (12.19)$$

$$\dot{m}_V \frac{d}{dr} (c_p T + \nu \mathcal{Q}x_O) = \frac{d}{dr} \left( 4\pi r^2 \rho D \frac{d}{dr} (c_p T + \nu \mathcal{Q}x_O) \right) \quad (12.20)$$

$$\dot{m}_V \frac{d}{dr} (x_V - \nu x_O) = \frac{d}{dr} \left( 4\pi r^2 \rho D \frac{d}{dr} (x_V - \nu x_O) \right) \quad (12.21)$$

Appropriate boundary conditions on these relations are (1) the droplet sur-

face heat flux condition 12.9, (2) zero droplet surface flux of non-fuel gases from equations 12.4 and 12.5, (3) zero oxidant flux at the droplet surface, (4) zero oxidant mass fraction at the droplet surface (5) temperature at the droplet surface,  $T_{r=R}$ , (6) known temperature far from the flame,  $T_{r=\infty}$ , (7) zero fuel/vapor mass fraction far from the flame,  $(x_V)_{r=\infty} = 0$ , and (8) a known oxidant mass fraction far from the flame,  $(x_O)_\infty$ . Using these conditions equations 12.19, 12.20 and 12.21 may be integrated twice to obtain:

$$\frac{\dot{m}_V}{4\pi\rho Dr} = \ln \left\{ \frac{c_p(T_{r=\infty} - T_{r=R}) + \mathcal{L} - \mathcal{Q}}{c_p(T - T_{r=R}) + \mathcal{L} - \mathcal{Q}(1 - x_V)} \right\} \quad (12.22)$$

$$\frac{\dot{m}_V}{4\pi\rho Dr} = \ln \left\{ \frac{c_p(T_{r=\infty} - T_{r=R}) + \mathcal{L} + \nu\mathcal{Q}(x_O)_{r=\infty}}{c_p(T - T_{r=R}) + \mathcal{L} + \nu\mathcal{Q}x_O} \right\} \quad (12.23)$$

$$\frac{\dot{m}_V}{4\pi\rho Dr} = \ln \left\{ \frac{1 + \nu(x_O)_{r=\infty}}{1 - x_V + \nu x_O} \right\} \quad (12.24)$$

and evaluating these expressions at the droplet surface leads to:

$$\frac{\dot{m}_V}{4\pi\rho DR} = \ln \left\{ \frac{c_p(T_{r=\infty} - T_{r=R}) + \mathcal{L} - \mathcal{Q}}{\mathcal{L} - \mathcal{Q}(1 - (x_V)_{r=R})} \right\} \quad (12.25)$$

$$\frac{\dot{m}_V}{4\pi\rho DR} = \ln \left\{ \frac{c_p(T_{r=\infty} - T_{r=R}) + \mathcal{L} + \nu\mathcal{Q}(x_O)_{r=\infty}}{\mathcal{L}} \right\} \quad (12.26)$$

$$\frac{\dot{m}_V}{4\pi\rho DR} = \ln \left\{ \frac{1 + \nu(x_O)_{r=\infty}}{1 - (x_V)_{r=R}} \right\} \quad (12.27)$$

and consequently the unknown surface conditions,  $T_{r=R}$  and  $(x_V)_{r=R}$  may be obtained from the relations

$$\begin{aligned} \frac{1 + \nu(x_O)_{r=\infty}}{1 - (x_V)_{r=R}} &= \frac{c_p(T_{r=\infty} - T_{r=R}) + \mathcal{L} + \nu\mathcal{Q}(x_O)_{r=\infty}}{\mathcal{L}} \\ &= \frac{c_p(T_{r=\infty} - T_{r=R}) + \mathcal{L} - \mathcal{Q}}{\mathcal{L} - \mathcal{Q}(1 - (x_V)_{r=R})} \end{aligned} \quad (12.28)$$

Having solved for these surface conditions, the evaporation rate,  $\dot{m}_V$ , would follow from any one of equations 12.25 to 12.27. However a simple, approximate expression for  $\dot{m}_V$  follows from equation 12.26 since the term  $c_p(T_{r=\infty} - T_{r=R})$  is generally small compared with  $\mathcal{Q}(x_V)_{r=R}$ . Then

$$\dot{m}_V \approx 4\pi R\rho D \ln \left( 1 + \frac{\nu\mathcal{Q}(x_O)_{r=\infty}}{\mathcal{L}} \right) \quad (12.29)$$

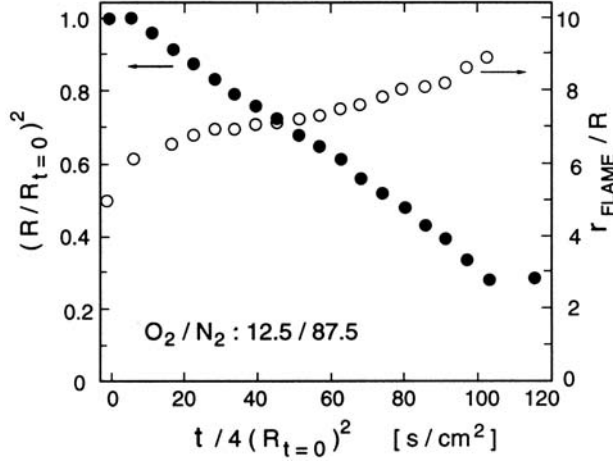


**Figure 12.14.** Droplet radius,  $R$ , and the ratio of the flame radius to the droplet radius,  $r_{flame}/R$ , for a burning octane droplet in a 12.5%  $O_2$ , 87.5%  $N_2$ ,  $0.15atm$  environment. Adapted from Law (1982).

The position of the flame front,  $r = r_{flame}$ , follows from equation 12.27 by setting  $x_V = x_O = 0$ :

$$r_{flame} = \frac{\dot{m}_V}{4\pi\rho D \ln(1 + \nu(x_O)_{r=\infty})} \approx R \frac{\ln(1 + \nu Q(x_O)_{r=\infty}/\mathcal{L})}{\ln(1 + \nu(x_O)_{r=\infty})} \quad (12.30)$$

As one might expect, the radius of the flame front increases rapidly at small oxygen concentrations,  $(x_O)_\infty$ , since this oxygen is quickly consumed. However, the second expression demonstrates that  $r_{flame}/R$  is primarily a function of  $Q/\mathcal{L}$ ; indeed for small values of  $(x_O)_{r=\infty}$  it follows that  $r_{flame}/R \approx Q/\mathcal{L}$ . We discuss the consequences of this in the next section.

Detailed reviews of the corresponding experimental data on single droplet combustion can be found in numerous texts and review articles including those listed above. Here we include just two sets of experimental results. Figure 12.14 exemplifies the data on the time history of the droplet radius,  $R$ , and the ratio of the flame radius to the droplet radius,  $r_{flame}/R$ . Note that after a small initial transient,  $R^2$  decreases quite linearly with time as explicitly predicted by equation 12.13 and implicitly contained in the combustion analysis. The slope,  $-d(R^2)/dt$ , is termed the *burning rate* and examples of the comparison between the theoretical and experimental burning rates are included in figure 12.15. The flame front location is also shown in figure 12.14; note that  $r_{flame}/R$  is reasonably constant despite the fivefold shrinkage of the droplet.

Further refinements of this simple analysis can also be found in the texts

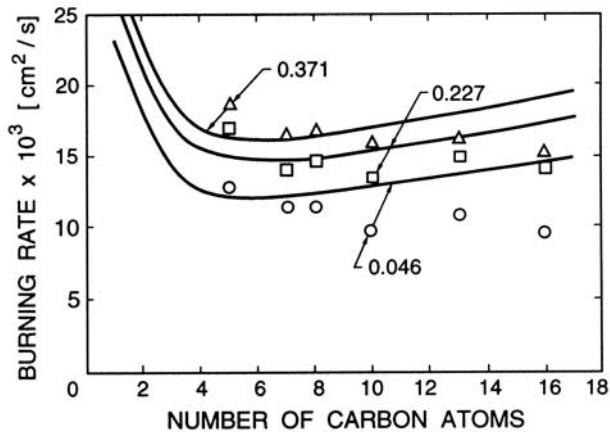


**Figure 12.15.** Theoretical and experimental burning rates,  $-d(R^2)/dt$  (in  $cm^2/s$ ), of various paraffin hydrocarbon droplets ( $R = 550\mu m$ ) in a  $T_{r=\infty} = 2530^\circ K$  environment with various mass fractions of oxygen,  $(x_O)_{r=\infty}$ , as shown. Adapted from Faeth and Lazar (1971).

mentioned previously. A few of the assumptions that require further analysis include whether or not the assumed steady state is pertinent, whether relative motion of the droplets through the gas convectively enhances the heat and mass transfer processes, the role of turbulence in modifying the heat and mass transfer processes in the gas, whether the chemistry can be modeled by a simple flame front, the complexity introduced by mixtures of liquids of different volatilities, and whether all the diffusivities can be assumed to be similar.

## 12.6 SPRAY COMBUSTION

Now consider the combustion of a spray of liquid droplets. When the radius of the flame front around individual droplets is small compared with the distance separating the droplets, each droplet will burn on its own surrounded by a flame front. However, when  $r_{flame}$  becomes comparable with the interdroplet separation the flame front will begin to surround a number of droplets and combustion will change to a form of droplet cloud combustion. Figure 12.16 depicts four different spray combustion scenarios as described by Chiu and Croke (1981) (see also Kuo 1986). Since the ratio of the flame front radius to droplet radius is primarily a function of the rate of the combustion heat release per unit mass of fuel to the latent heat of vaporization of the fuel, or  $Q/\mathcal{L}$  as demonstrated in the preceding section, these patterns of droplet cloud combustion occur in different ranges of that parameter. As

depicted in figure 12.16(a), at high values of  $Q/\mathcal{L}$ , the flame front surrounds the entire cloud of droplets. Only the droplets in the outer shell of this cloud are heated sufficiently to produce significant evaporation and the outer flow of this vapor fuels the combustion. At somewhat lower values of  $Q/\mathcal{L}$  (figure 12.16(b)) the entire cloud of droplets is evaporating but the flame front is still outside the droplet cloud. At still lower values of  $Q/\mathcal{L}$  (figure 12.16(c)), the main flame front is within the droplet cloud and the droplets in the outer shell beyond that main flame front have individual flames surrounding each droplet. Finally at low  $Q/\mathcal{L}$  values (figure 12.16(d)) every droplet is surrounded by its own flame front. Of course, several of these configurations may be present simultaneously in a particular combustion process. Figure 12.17 depicts one such circumstance occurring in a burning spray emerging from a nozzle.

Note that though we have focused here on the combustion of liquid droplet

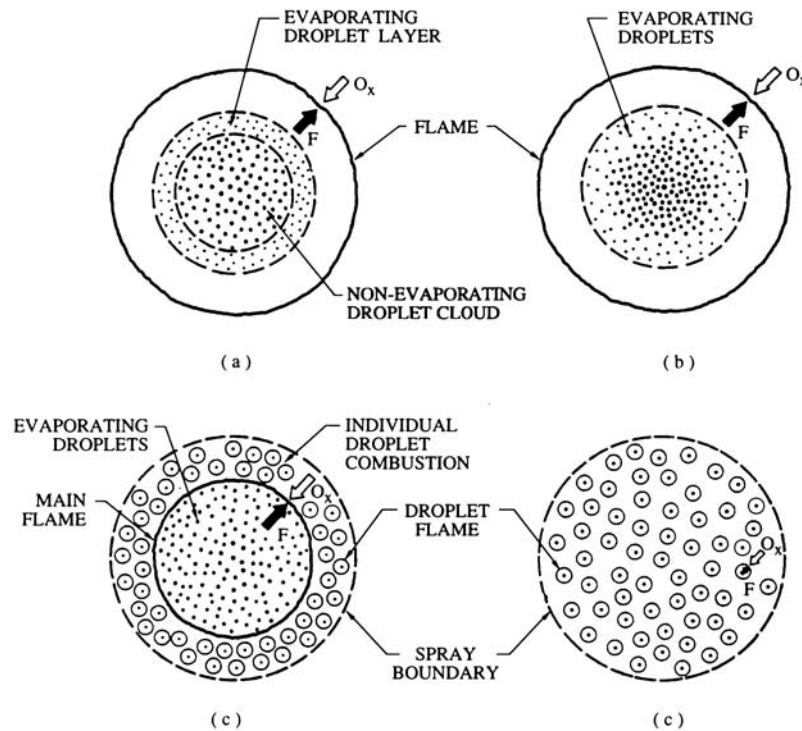


**Figure 12.16.** Four modes of droplet cloud combustion: (a) Cloud combustion with non-evaporating droplet core (b) Cloud combustion with evaporating droplets (c) Individual droplet combustion shell (d) Single droplet combustion. Adapted from Chiu and Croke (1981).

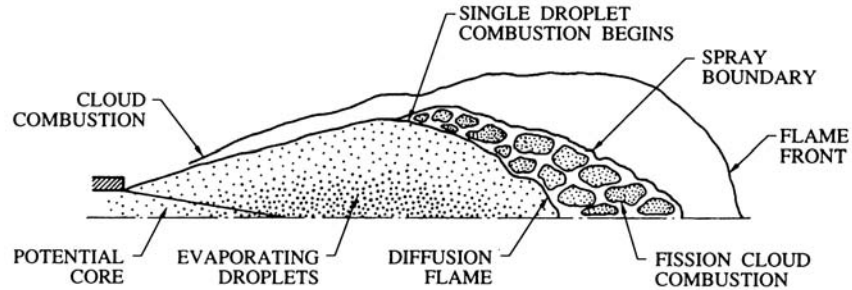


**Figure 12.17.** An example of several modes of droplet cloud combustion in a burning liquid fuel spray. Adapted from Kuo (1986).

sprays, the combustion of suspended solid particles is of equal importance. Solid fuels in particulate form are burned both in conventional boilers where they are injected as a dusty gas and in fluidized beds into which granular particles and oxidizing gas are continuously fed. We shall not dwell on solid particle combustion since the analysis is very similar to that for liquid droplets. Major differences are the boundary conditions at the particle surface where the devolatilization of the fuel and the oxidation of the char require special attention (see, for example, Gavalas 1982, Flagan and Seinfeld 1988).